

CONSTRAINTS ON THE SHAPE OF THE MILKY WAY DARK MATTER HALO FROM THE SAGITTARIUS STREAM

CARLOS VERA-CIRO^{1,2} & AMINA HELMI²
Draft version July 29, 2013

ABSTRACT

We propose a new model for the dark matter halo of the Milky Way that fits the properties of the stellar stream associated with the Sagittarius dwarf galaxy. Our dark halo is oblate with $q_z = 0.9$ for $r \lesssim 10$ kpc, and can be made to follow the Law & Majewski model at larger radii. However, we find that the dynamical perturbations induced by the Large Magellanic Cloud on the orbit of Sgr cannot be neglected when modeling its streams. When taken into account, this leads us to constrain the Galaxy's outer halo shape to have minor-to-major axis ratio $(c/a)_\Phi = 0.8$ and intermediate-to-major axis ratio $(b/a)_\Phi = 0.9$, in good agreement with cosmological expectations.

Subject headings: galaxies: dwarf - galaxies: interactions - Local Group

1. INTRODUCTION

The stellar stream associated with the Sagittarius (Sgr) dwarf galaxy has been extensively used to probe the mass distribution of the Milky Way (MW), particularly its dark halo. Despite many attempts, there is currently no fully satisfactory model of its shape based on the dynamics of the stream. Extreme oblate configurations have been ruled out (Ibata et al. 2001), while the tilt of the orbital plane has been shown to require a mildly oblate halo by Johnston, Law & Majewski (2005). On the other hand, the line-of-sight velocities call for a prolate halo (Helmi 2004). This conundrum led (Law & Majewski 2010, hereafter LM10) to propose a triaxial dark halo for the MW, with axis ratios $(c/a)_\Phi = 0.72$ and $(b/a)_\Phi = 0.99$ (see also Deg & Widrow 2012). This model fits well all positional and kinematic information available.

Although the halos assembled in Λ CDM are triaxial (Jing & Suto 2002; Allgood et al. 2006; Schneider, Frenk & Cole 2012), the configuration proposed by LM10 is rare: the halo is close to oblate, with a much smaller c/a than predicted in cosmological simulations for MW mass halos, which have $\langle c/a \rangle_\Phi = 0.9pm0.1$ over the relevant distance range (i.e., that probed by the Sgr stream Hayashi, Navarro & Springel 2007), and difficult to understand from a physical point of view (its minor axis points almost toward the Sun, while the intermediate axis is perpendicular to the Galactic disk). Furthermore, the presence of the disk is expected to lead to a change in the inner halo shape toward a more oblate configuration (Bryan et al. 2013). Finally, the disk's stability is not naturally ensured in the LM10 potential, as there are no tube orbits around the intermediate axis (Debattista et al. 2013).

In this Letter we take a fresh look at determining the shape of the MW halo from the Sgr streams' dynamics. We consider the possibility that the shape of the halo varies with distance from the Galactic center, as expected in Λ CDM (Vera-Ciro et al. 2011). Evidence suggesting a halo with non-constant axis ratios has been reported by Banerjee & Jog (2011) using the flaring of the HI layer of the MW disk. We present a new model that takes into account the effect of a baryonic disk in Section 2. Because of the cosmological rareness of the LM10 model, in Sectio 3 we explore the possibility that the dynamics of the Sgr stream may be explained through the combined effect of

the Large Magellanic Cloud (LMC) and a less axisymmetric, but more triaxial, outer halo. In that section we show that these models provide equally good fits to the dynamics of the young Sgr streams as the LM10 potential, and that older wraps may be used to distinguish amongst them. We finalize with a brief summary in Section 4.

2. INNER HALO: ACCOUNTING FOR THE EFFECT OF THE GALACTIC DISK ON THE HALO SHAPE

Next we present the characteristics of our Galactic potential, which includes a halo whose shape by construction is oblate in the center and triaxial at large radii. We then show the results of orbital integrations in this potential aimed at reproducing the properties of the Sgr stream.

2.1. Description of the Potential

We model the Galactic potential with three components: a disk, a spherical bulge and a dark matter halo. The disk and bulge follow, respectively a Miyamoto-Nagai distribution ($M_{\text{disk}} = 10^{11} M_\odot$, $a = 6.5$ kpc, $b = 0.26$ kpc; Miyamoto & Nagai 1975), and a Hernquist spheroid ($M_{\text{bulge}} = 3.4 \times 10^{10} M_\odot$, $c = 0.7$ kpc; Hernquist 1990).

Based on the arguments presented in the Introduction, we seek a halo potential that satisfies the following.

1. It is axisymmetric in the inner parts. This will guarantee the stability of the disk, as well as account for the effects of the baryonic disk on the dark halo.
2. It is triaxial in the outskirts, and follows the LM10 model.
3. It has a smooth transition between these two regimes.

We choose to model such a profile using a modification of the algorithm presented by Vogelsberger et al. (2008). Consider the spherical potential

$$\Phi_s(r) = v_{\text{halo}}^2 \ln(r^2 + d^2). \quad (1)$$

The geometrical properties of the potential are encapsulated in the variable $r = (x^2 + y^2 + z^2)^{1/2}$. A replacement that satisfies the above requirements is $r \rightarrow \tilde{r}$, with

$$\tilde{r} \equiv \frac{r_a + r_T}{r_a + r_A} r_A, \quad (2)$$

² Department of Astronomy, University of Wisconsin, 2535 Sterling Hall, 475 N. Charter Street, Madison, WI 53076, USA. e-mail: ciro@astro.wisc.edu

² Kapteyn Astronomical Institute, University of Groningen, P.O.Box 800, 9700 AV Groningen, The Netherlands.

where r_A and r_T are ellipsoidal radii (as described below). For small distances $r_A, r_T \ll r_a$ then $\tilde{r} \approx r_A$, and similarly for large distances $r_A, r_T \gg r_a$ then $\tilde{r} \approx r_T$. In particular,

$$r_A^2 \equiv x^2 + y^2 + \frac{z^2}{q_z^2} = R^2 + \frac{z^2}{q_z^2}, \quad (3)$$

$$r_T^2 \equiv C_1 x^2 + C_2 y^2 + C_3 xy + \frac{z^2}{q_3^2}, \quad (4)$$

and,

$$C_1 = \frac{a_1^2}{q_1^2} + \frac{a_2^2}{q_2^2}, \quad C_2 = \frac{a_1^2}{q_2^2} + \frac{a_2^2}{q_1^2}, \quad C_3 = 2a_1 a_2 \left(\frac{1}{q_1^2} - \frac{1}{q_2^2} \right), \quad (5)$$

where $a_1 = \cos \phi$ and $a_2 = \sin \phi$, and $\phi = 97^\circ$. Therefore, the properties of the mass distribution are encoded in the quantities r_A and r_T , with the latter defined as in LM10. The Sun is assumed to be located at $x = -R_\odot$, and the z -axis to point perpendicular to the disk. The resulting potential,

$$\Phi_{\text{halo}}(x, y, z) = \Phi_s(\tilde{r}(x, y, z)), \quad (6)$$

is axisymmetric at small radii, and triaxial in the outskirts.

Figure 1 shows different slices of the resulting potential. Here we have chosen the flattening of the axisymmetric part to be $q_z = 0.9$ (as in, e.g., Johnston, Law & Majewski 2005). The axis ratios for the triaxial component (q_1, q_2, q_3), and its tilt ϕ , are taken from the LM10 model. v_{halo} is set to ensure that $v_{\text{circ}}(R_\odot = 8 \text{ kpc}) = 225.2 \text{ km s}^{-1}$. The transition radius, $r_a = 30 \text{ kpc}$, is selected such that the region of dominance of the disk resides inside the axisymmetric part of the halo potential. However, the effective transition between the axisymmetric and triaxial regions occurs at a smaller radius, $\approx 10 \text{ kpc}$.

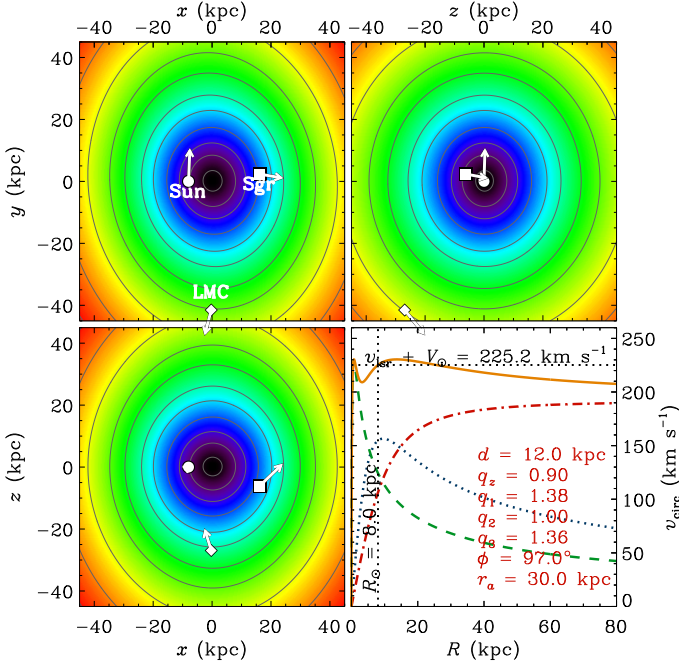


FIG. 1.— Dark halo potential isocontours on the plane $z = 0$ (top left), $y = 0$ (bottom left) and $x = 0$ (top right). For reference, we have included the positions and directions of motion for the Sun (circle), Sgr (square), and the LMC (diamond). The bottom right panel shows the circular velocity profile v_{circ} for the disk (dotted blue), bulge (dashed green), and halo (dash-dotted red). The halo makes a transition from oblate to triaxial at $r_a = 30 \text{ kpc}$.

2.2. Generating the stream

In what follows, we work on the assumption that the orbit of the center of mass traces the arms of the stream. Although this is not strictly true (Eyre & Binney 2009), it represents a reasonable first approximation (Law & Majewski 2010). With this caveat, we proceed to integrate test particles in the composite potential described above. For each particle, we generate a set of initial conditions consistent with the present-day six-dimensional (6D) phase-space coordinates of the Sgr dwarf galaxy. More specifically, we sample each observable from a Gaussian distribution, with its mean and variance taken from the literature. The position is assumed to be at $(l, b) = (5^\circ.6, -14^\circ.2)$ (Majewski et al. 2003), the heliocentric distance $d = 25 \pm 2 \text{ kpc}$ (Kunder & Chaboyer 2009), the line-of-sight velocity $v_r = 140 \pm 2 \text{ km s}^{-1}$ (Ibata et al. 1997), and the proper motions $(\mu_l \cos b, \mu_b) = (-2.4 \pm 0.2, 2.1 \pm 0.2) \text{ mas yr}^{-1}$ (Dinescu et al. 2005). Orbits are integrated forward and backward in time for 2 Gyr, to generate the set of observables associated with the leading and trailing arms, respectively.

For each integrated orbit, we take 10 samples of the form $\{\mathbf{x}(t_i), \mathbf{v}(t_i)\}_{i=1}^{10}$, where the times t_i are randomly selected between $t = 0$ and the maximum time of integration t_{max} . t_{max} is the time that it takes the orbit to complete one wrap in the sky, and is typically $\sim 1 \text{ Gyr}$. The full 6D information contained in each sample is transformed into the set of observables often used to represent the stream: position on the sky (Λ_\odot, B_\odot) (Majewski et al. 2003), heliocentric distance d , line-of-sight velocity in the Galactic standard of rest v_{gsr} , and proper motions $(\mu_b, \mu_l \cos b)$.

In total 5×10^4 initial conditions are integrated, producing 5×10^5 points in the space of observables, which are assigned to a grid using the Cloud in Cell algorithm (Hockney & Eastwood 1988). Figure 2 shows the projected density for different observables as a function of Λ_\odot : $P(o, \Lambda_\odot)$, with $o = \{v_{\text{gsr}}, B_\odot, d, \mu_b, \mu_l \cos b\}$. In each panel, we marginalize the density over the observed quantity o at fixed Λ_\odot , that is $P(o|\Lambda_\odot) = \int do P(o, \Lambda_\odot)$. The solid black line shows the median of $P(o|\Lambda_\odot)$, and with gray bands we represent the 1σ and 2σ equivalent scatter around the median.

For comparison we have included the mean orbit of the LM10 model (orange dashed line) and their N -body run (green dots). We have also added the measurements of (Majewski et al. 2004, cyan stars), (Correnti et al. 2010, magenta triangles) and (Carlin et al. 2012, red diamonds). As expected (Binney 2008; Eyre & Binney 2009), there are some deviations between the mean orbit and the location of the tidal stream as probed by the N -body run, for example, in the distances d of the trailing arm.

Figure 2 shows that the radial velocities v_{gsr} , distances, and the positions in the sky B_\odot are well fit in our new potential, and as well as in the LM10 model. In test runs we found that the dependence of the fits on the parameter r_a is not strong, whenever this is kept within reasonable values. Of course, a value of $r_a \gg r_{\text{apo}}$ (with r_{apo} the apocenter distance of the orbit of the Sgr dwarf) will lead to potential that is purely oblate in the region probed by the stream, and therefore will not be able to fit the velocities of the leading arm.

The dependence on the flattening q_z , is shown in Figure 3 for the leading arm (the trailing arm is rather insensitive in the region where observations are available). We explore four different values of $q_z = \{0.7, 0.8, 0.9, 1.1\}$ keeping $r_a = 30 \text{ kpc}$. In the regions probed by the data, $\Lambda_\odot \gtrsim 200^\circ$, the effect of changing q_z is strong on the velocities, which clearly rule out

$q_z < 0.9$. On the other hand, the positions on the sky disfavor $q_z > 1$. In general, we find that $0.90 < q_z < 0.95$ yield good fits to the observables in the leading arm. Therefore, Figure 3 shows that the inner halo shape has an effect on the Sgr stream, even though the orbit mainly probes the triaxial regime of the potential.

3. OUTER HALO: THE EFFECT OF LMC

It is very intriguing that the direction of the major axis of the LM10 potential approximately lies in the direction toward the LMC. This suggests that the LM10 potential may perhaps be seen as an effective field: the result of the combined potentials of the LMC and of a truly triaxial MW halo.

Let us consider the various torques exerted on the (instantaneous) plane of motion of Sgr. First, note that since $\phi \approx 90^\circ$, the principal axes of the potential of the halo are nearly aligned with the Galactocentric coordinate system. Consequently, we can simplify Equation (4) to

$$\tilde{r}^2 \approx x^2 + \frac{y^2}{q_1^2} + \frac{z^2}{q_3^2}. \quad (7)$$

The torque induced by the LM10 potential is simply $\boldsymbol{\tau} = -\mathbf{r} \times \partial\Phi_{\text{halo}}/\partial\mathbf{r}$. Of the three components of this field, the x - and z - components are controlled by gradient of the force along the y - direction, i.e., that of the major axis of the LM10 halo. Consider, for instance, the z component,

$$\begin{aligned} \tau_z^{\text{halo}} &= -\frac{\partial\Phi_{\text{halo}}}{\partial\tilde{r}} \frac{xy}{\tilde{r}} \left(\frac{1}{q_1^2} - 1 \right) \approx -\frac{v_{\text{circ}}^2}{\tilde{r}^2} xy \left(\frac{1}{q_1^2} - 1 \right) \\ &\approx -\frac{GM_{\text{halo}}(\tilde{r})}{\tilde{r}^3} xy \left(\frac{1}{q_1^2} - 1 \right). \end{aligned} \quad (8)$$

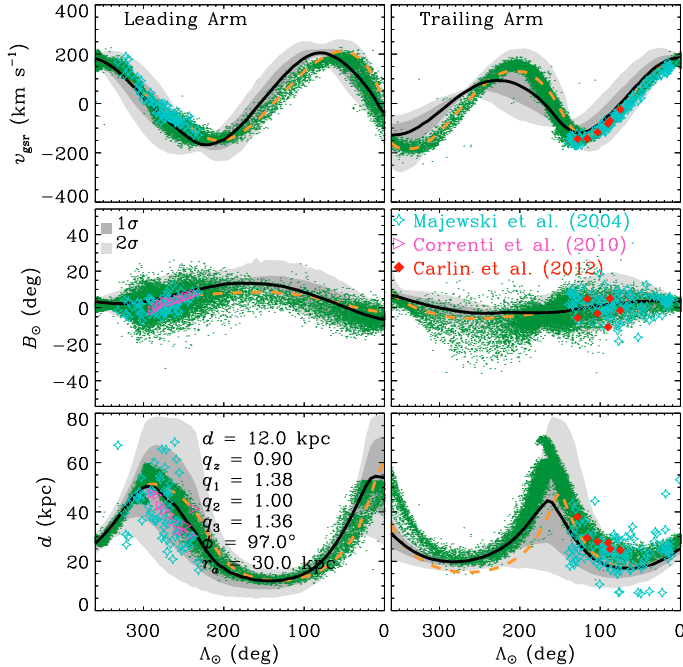


FIG. 2.— Radial velocity v_{gr} , position in the sky B_\odot , and heliocentric distance d as function of the angular distance along the stream Λ_\odot for the leading arm (left) and trailing arm (right) for the potential described in Figure 1. The solid black line is the median orbit and the shaded regions represent 1σ and 2σ equivalent dispersion. The green points are from the N -body simulation by LM10, while their center of mass orbit is the orange dashed curve.

In our reference system, the present-day position of the LMC is nearly on the plane $x = 0$ (see Figure 1). The force generated at $\mathbf{r} = xi + yj + zk$ by a point mass M_{LMC} at the position of the LMC, \mathbf{r}_{LMC} , is

$$\mathbf{F}_{\text{LMC}} = -GM_{\text{LMC}} \frac{\mathbf{r} - \mathbf{r}_{\text{LMC}}}{|\mathbf{r} - \mathbf{r}_{\text{LMC}}|^3}, \quad (9)$$

which generates a torque $\boldsymbol{\tau}^{\text{LMC}} = \mathbf{r} \times \mathbf{F}_{\text{LMC}}$, whose z -component is

$$\tau_z^{\text{LMC}} = -\frac{GM_{\text{LMC}}}{|\mathbf{r} - \mathbf{r}_{\text{LMC}}|^3} (y x_{\text{LMC}} - x y_{\text{LMC}}) \approx \frac{GM_{\text{LMC}} x y_{\text{LMC}}}{|\mathbf{r} - \mathbf{r}_{\text{LMC}}|^3}. \quad (10)$$

Using Equations (8) and (10) we can quantify the relative amplitude of the torques exerted by the triaxial halo and by the LMC on the orbit of Sgr at its present location:

$$\frac{\tau_z^{\text{LMC}}}{\tau_z^{\text{halo}}} \sim \frac{M_{\text{LMC}}}{M_{\text{halo}}(\tilde{r})} \frac{\tilde{r}^3}{r_{\text{sgr/LMC}}^3} \frac{y_{\text{LMC}}}{y} \frac{1}{1/q_1^2 - 1}. \quad (11)$$

The mass of the LM10 halo enclosed at the present distance of Sgr is $M_{\text{halo}} \sim 10^{11} M_\odot \approx M_{\text{LMC}}$ (Besla et al. 2010). At the present day $\tilde{r}/r_{\text{sgr/LMC}} \sim 0.5$, while $y_{\text{LMC}}/y \sim 10$, and taking $q_1 = 1.38$, this implies that the expression above is of order unity. Additionally, since $q_1 > 1$ the torque generated by the LMC points in the same direction of that induced by the triaxial halo ($y_{\text{LMC}} < 0$, cf. Figure 1). This means that presently the torque on Sgr generated by the LMC is as important as the one generated by the triaxial halo.

To confirm this order of magnitude argument we perform new orbital integrations in a slightly modified halo model, which is still given by Equation (6) but now with axis ratios $q_1 = 1.1$, $q_2 = 1.0$, and $q_3 = 1.25$, and where we kept the orientation $\phi = 97^\circ$. This corresponds to a minor-to-major axis ratio $(c/a)_\Phi = 0.8$ and intermediate-to-major axis ratio $(b/a)_\Phi = 0.9$, which are consistent with current predictions of dark matter only simulations of MW type halos (Hayashi, Navarro & Springel 2007). We also include the

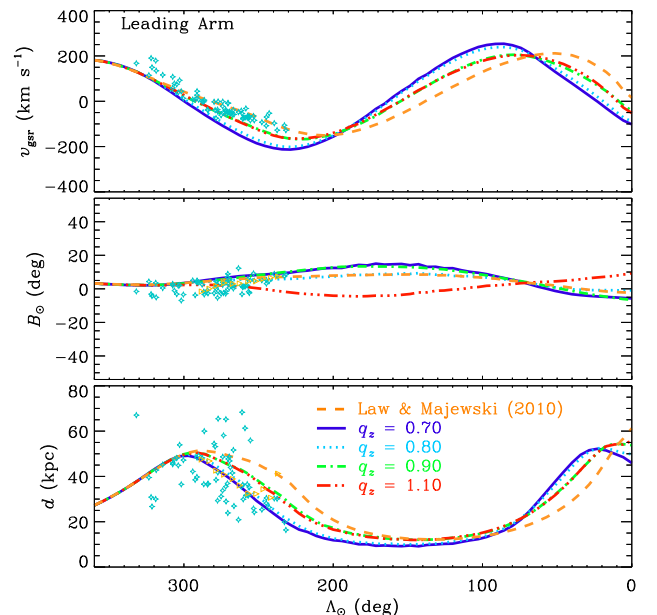


FIG. 3.— Leading arm line-of-sight velocities (top), position on the sky (middle), and heliocentric distances (bottom) for different q_z and $r_a = 30 \text{ kpc}$. The potential for $r \gg r_a$ is the same triaxial model as in Figure 2. The dashed orange line is the mean orbit of LM10.

potential of the LMC. To this end, we evolve backward and forward the orbit of the LMC, from its present day position $(\alpha, \delta) = (5^{\text{h}}, 27^{\text{m}}.6, -69^{\circ}, 52'.2)$ (Piatek, Pryor & Olszewski 2008), heliocentric distance $d = 50.1$ kpc (Freedman et al. 2001), proper motions $(\mu_l \cos b, \mu_b) = (1.96, 0.44)$ mas yr $^{-1}$ (Piatek, Pryor & Olszewski 2008) and line-of-sight velocity $v_r = 270$ km s $^{-1}$ (van der Marel et al. 2002). We then place a Hernquist sphere of mass $M_{\text{LMC},0} = 8 \times 10^{10} M_{\odot}$ and scale radius $r_{\text{LMC},0} = 2$ kpc along this orbit.

Figure 4 shows a model of the Sgr stream orbital path in which the LMC and our slightly revised halo are included. As before we show the LM10 model with the dashed orange line. It is interesting to note that after including the LMC, the orbital tilt of the leading arm is well fit despite the change in shape of the MW halo, which is now elongated in the z -direction at large radii. The torque of the orbital plane is also felt by the trailing arm, resulting on a slight change in the direction of gradient of B_{\odot} for $\Lambda \lesssim 100^{\circ}$.

This analysis shows that the perturbations of the LMC on the orbit of the Sgr stream are non-negligible, and implies that previously estimated values of the axis ratios of the MW dark matter potential from models that have omitted this perturbation may be biased. For example, $(c/a)_{\Phi} = 0.8$ for the model presented in Figure 4, with the LMC included, while the LM10 model has $(c/a)_{\Phi} = 0.72$.

In a more realistic scenario including dynamical friction, the LMC might have been even more massive than at present day and its role in shaping the orbit of Sgr even more important. However, some caution is necessary before drawing strong conclusions about the dynamics of the stream 3-4 Gyr ago. For example, if the LMC is in its first infall, in which case the closest

encounter with the Sgr dwarf galaxy is currently taking place. However, during the last ~ 2 Gyr its presence could have significantly affected older wraps of the Sgr stream.

We explore in Figure 5 how the differences between the various models may become apparent for older portions of the stream. Here we show the first (solid) and second (dotted) wraps of the leading (left) and trailing (right) arms, for the three different models discussed so far: black is our fiducial model from Section 2; green is the model that includes the LMC and red; is the LM10 triaxial model. We have included observations of different stellar tracers: RR Lyraes (Ivezić et al. 2000; Vivas, Zinn & Gallart 2005; Prior, Da Costa & Keller 2009), carbon giants (Ibata et al. 2001), red giant branch stars (Dohm-Palmer et al. 2001; Starkenburg et al. 2009; Correnti et al. 2010), M giants (Majewski et al. 2004) and red horizontal branch stars (Shi et al. 2012). It should be noted that Shi et al. (2012) preselect their sample according to the LM10 model.

We show also the positions in the sky for the bright (orange filled squares) and the faint (orange open squares) streams in the Southern Galactic hemisphere from Koposov et al. (2012). Whereas the association to the trailing arm is clear for the brighter portion of the stream, the faint parallel stream could perhaps be an older wrap from either trailing or leading arm. More information, especially kinematic, is necessary to disentangle the various contributions of Sgr in this region, and these might also help constrain further the shape of the dark halo of the MW. It should be borne in mind that although the differences between older wraps amongst the various models are larger than for younger streams, the predictions for their properties are clearly much more uncertain.

4. CONCLUSIONS

In this Letter we have presented a new model for the MW dark matter halo that fits the observations of the Sgr stream, both the radial velocities as well as the orbital tilt of the leading arm. The dark halo potential is axisymmetric and flattened toward the disk plane for $r \lesssim 10$ kpc, with $q_z = 0.9$, and asymptotically approaches the Law & Majewski (2010) triaxial model at larger radii. A gratifying property of this potential is that its inner oblate shape and orientation account for the presence of the Galactic disk and ensure its stability.

The triaxial part of this potential, however is not entirely consistent with expectations from the Λ CDM model. Its odd (nearly oblate) configuration can be changed, and brought to a more cosmologically plausible shape, if the gravitational field generated by the LMC is taken into account. The integration of orbits in a composite potential including the LMC and an outer triaxial halo with $q_1 = 1.10$, $q_2 = 1.00$ and $q_3 = 1.25$ (that is, as before, oblate in the inner regions) is also found to reproduce well the properties of the Sgr streams in the region where these have been constrained observationally.

The conclusions drawn in this work are based on heuristic searches of the high-dimensional parameter space that characterizes the gravitational potential of the MW and that of the LMC. By no means do they represent best-fit models in a statistical sense. Therefore, the predictions made cannot be considered exclusive or definitive, but serve to guide where future observations could focus to distinguish between various models. Notwithstanding these caveats, we have been able to demonstrate that the dynamics of the Sgr streams can be understood in a context that is consistent with expectations from Λ CDM.

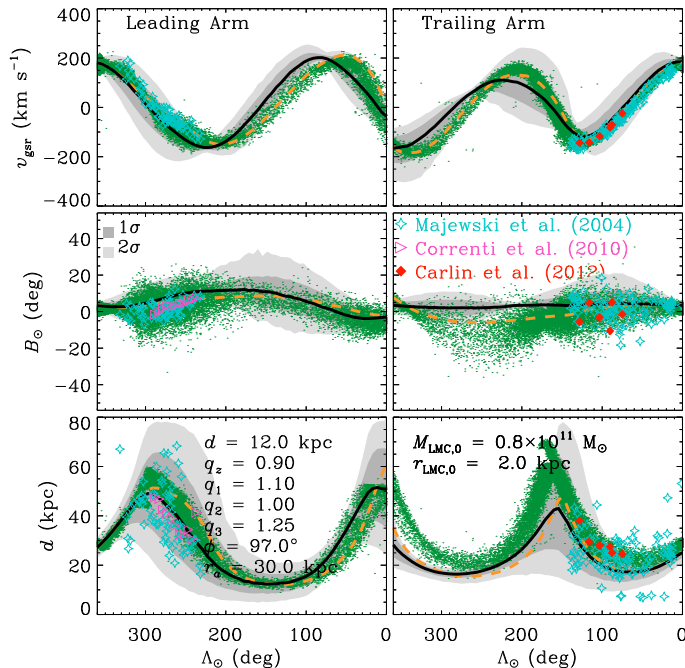


FIG. 4.— Radial velocity v_{gr} , position in the sky B_{\odot} , heliocentric distance d and proper motions $\mu_l \cos b, \mu_b$ as a function of the angular distance along the stream Λ_{\odot} for the leading arm (left) and the trailing arm (right). The potential used includes the LMC as well as that for the halo, which has the form described in Equations. (2)–(6), i.e., it is oblate in the center with $q_z = 0.9$ and $r_a = 30$ kpc, but with axis ratios $q_1 = 1.1$, $q_2 = 1.0$, and $q_3 = 1.25$.

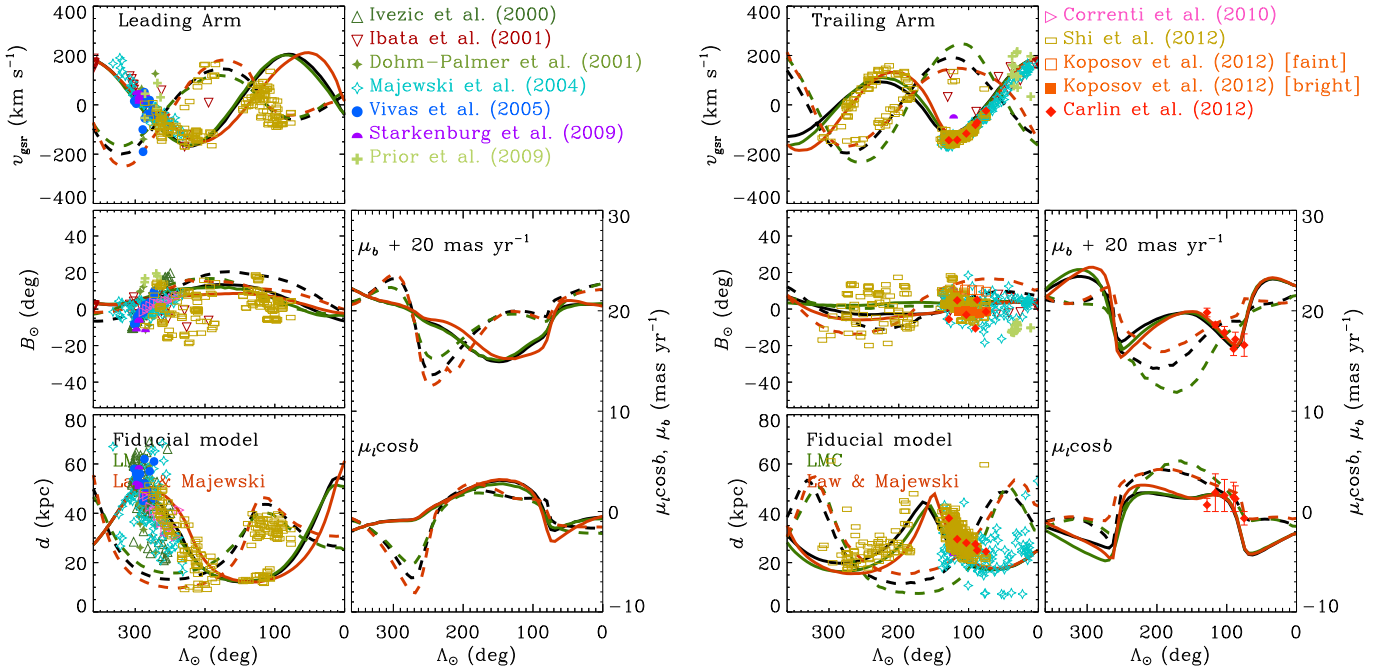


FIG. 5.— First and second wraps of the leading and trailing streams from Sgr for the different models explored: black is our fiducial model from Section 2, green is the model that includes the LMC and red is the LM10 triaxial model.

ACKNOWLEDGMENTS

We are grateful for the financial support from the European Research Council under ERC-StG grant GALACTICA-240271.

REFERENCES

- Allgood B., Flores R. A., Primack J. R., Kravtsov A. V., Wechsler R. H., Faltenbacher A., Bullock J. S., 2006, *MNRAS*, 367, 1781
 Banerjee A., Jog C. J., 2011, *ApJ*, 732, L8
 Besla, G. and Kallivayalil, N. and Hernquist, L. and van der Marel, R. P. and Cox, T. J. and Kereš, D., 2010, *ApJ*, 721, 97
 Binney, J., 2008, *MNRAS*, 386, L47
 Bryan S. E., Kay S. T., Duffy A. R., Schaye J., Dalla Vecchia C., Booth C. M., 2013, *MNRAS*, 429, 3316
 Carlin J. L., Majewski S. R., Casetti-Dinescu D. I., Law D. R., Girard T. M., Patterson R. J., 2012, *ApJ*, 744, 25
 Correnti M., Bellazzini M., Ibata R. A., Ferraro F. R., Varghese A., 2010, *ApJ*, 721, 329
 Debattista V. P., Roskar R., Valluri M., Quinn T., Moore B., Wadsley J., 2013, *arXiv:1301.2670*
 Deg N., Widrow L., 2012, *MNRAS*, 428, 912
 Dinescu D. I., Girard T. M., van Altena W. F., López C. E., 2005, *ApJ*, 618, L25
 Dohm-Palmer R. C. et al., 2001, *ApJ*, 555, L37
 Eyre A., Binney J., 2009, *MNRAS*, 400, 548
 Freedman W. L. et al., 2001, *ApJ*, 553, 47
 Hayashi E., Navarro J. F., Springel V., 2007, *MNRAS*, 377, 50
 Helmi A., 2004, *ApJ*, 610, L97
 Hernquist L., 1990, *ApJ*, 356, 359
 Hockney R. W., Eastwood J. W., 1988, *Computer simulation using particles*. Taylor & Francis
 Ibata R., Lewis G. F., Irwin M., Totten E., Quinn T., 2001, *ApJ*, 551, 294
 Ibata R. A., Wyse R. F. G., Gilmore G., Irwin M. J., Suntzeff N. B., 1997, *AJ*, 113, 634
 Ivezić Ž. et al., 2000, *AJ*, 120, 963
 Jing Y. P., Suto Y., 2002, *ApJ*, 574, 538
 Johnston K. V., Law D. R., Majewski S. R., 2005, *ApJ*, 619, 800
 Koposov S. E. et al., 2012, *ApJ*, 750, 80
 Kunder A., Chaboyer B., 2009, *AJ*, 137, 4478
 Law D. R., Majewski S. R., 2010, *ApJ*, 714, 229 (LM10)
 Majewski S. R., Skrutskie M. F., Weinberg M. D., Ostheimer J. C., 2003, *ApJ*, 599, 1082
 Majewski S. R. et al., 2004, *AJ*, 128, 245
 Miyamoto M., Nagai R., 1975, *PASJ*, 27, 533
 Piatek S., Pryor C., Olszewski E. W., 2008, *AJ*, 135, 1024
 Prior S. L., Da Costa G. S., Keller S. C., 2009, *ApJ*, 704, 1327
 Starkenburg E. et al., 2009, *ApJ*, 698, 567
 Schneider M. D., Frenk C. S., Cole S., 2012, *J. Cosmology Astropart. Phys.*, 5, 30
 Shi W. B., Chen Y. Q., Carrell K., Zhao G., 2012, *ApJ*, 751, 130
 van der Marel, R. P. and Alves, D. R. and Hardy, E. and Suntzeff, N. B., 2002, *ApJ*, 124, 2639
 Vera-Ciro C. A., Sales L. V., Helmi A., Frenk C. S., Navarro J. F., Springel V., Vogelsberger M., White S. D. M., 2011, *MNRAS*, 416, 1377
 Vivas A. K., Zinn R., Gallart C., 2005, *AJ*, 129, 189
 Vogelsberger M., White S. D. M., Helmi A., Springel V., 2008, *MNRAS*, 385, 236